High Sensitivity Planar Hall Effect Magnetic Field Gradiometer for Measurements in Millimeter Scale Environments

Hariharan Nhalil [1], Moty Schultz [1], Shai Amrusi [2], Asaf Grosz [2] and Lior Klein [1,*]

[1] Department of Physics, Institute of Nanotechnology and Advanced Materials, Bar-Ilan University, Ramat-Gan 52900, Israel
[2] Department of Electrical and Computer Engineering, Ben-Gurion University of the Negev, P.O. Box 653, Beer-Sheva 84105, Israel
* Correspondence: Lior.Klein@biu.ac.il

Abstract: We report a specially designed magnetic field gradiometer based on a single elliptical planar Hall effect (PHE) sensor, which allows measuring magnetic field at nine different positions in a 4 mm length scale. The gradiometer detects magnetic field gradients with equivalent gradient magnetic noises of $\sim$958, $\sim$192, $\sim$51, and $\sim$26 nT/m$\sqrt{}$Hz (pT/mm$\sqrt{}$Hz) at 0.1, 1, 10, and 50 Hz, respectively. The performance of the gradiometer is tested in ambient conditions by measuring the field gradient induced by electric currents driven in a long straight wire. This gradiometer is expected to be highly useful for the measurement of magnetic field gradients in confined areas for its small footprint, low noise, scalability, simple design, and low costs.

Keywords: planar hall effect; gradiometer; magnetic sensor

1. Introduction

The detection of magnetic field gradients is important for many applications, including geomagnetic mapping [1,2], magnetic navigation [3,4], current sensing [5,6], medical diagnosis [7,8], etc. To perform detections in confined spaces, especially where the compact form factor is highly important (e.g., any portable [9] or wearable electronic devices [10–12], body implants [13], etc.), the sensors should have low equivalent magnetic noise and a small footprint as the minimum baseline (the distance between two sensors) of the gradiometer is decided by its footprint. Although there are gradiometers that can quantify the field gradient by measuring the magnetic field only at a single point [14], commonly, the determination of the magnetic field gradient requires magnetic field measurements at two or more locations.

Planer Hall effect sensors have the features required for confined space gradiometry: small footprint and high field resolution. Compared to other magnetoresistive sensors, they exhibit very low equivalent magnetic noise (EMN or resolution), especially at very low frequencies [15–17]. Previously, EMNs of $\sim$5 pT/$\sqrt{}$Hz at 10 Hz and less than 25 pT/$\sqrt{}$Hz at 50 Hz were reported for elliptical PHE sensors with and without magnetic flux concentrators (MFCs), respectively [16,17]. Here, the area of the magnetic ellipse with a major axis length of 5 mm (aspect ratio of 1/6) without MFCs is only $\sim$5 mm^2, whereas for high-resolution sensors such as superconducting quantum interference device (SQUID) magnetometers [18] or conventional fluxgate magnetometers [19], they have at least a one-order higher footprint, which makes them unsuitable for many confined space measurements. Moreover, some of these high-resolution magnetometers are operated at cryogenic temperatures and require bulky instrumentation. PHE sensors on the other hand are known for their room temperature operation, low temperature dependence [20], simple design and fabrication, linearity, and portability. These important characteristics make them ideal for gradiometer applications in confined spaces.

Here, we discuss the fabrication and testing of a specially designed elliptical planar Hall effect gradiometer (EPHEG) with nine sensing positions in a 4 mm length scale and a footprint less than 5 mm^2. Since the excitation current is shared by all sensing positions, the power consumption is 9 times smaller than the power needed to operate nine separate sensors. Moreover, the EPHEG can be used in smaller volumes than nine separate elliptical sensors and has redundancy in case one voltage pair fails during a measurement. Our EPHEG presents low equivalent gradient magnetic noises of ~958, ~192, ~51, and ~26 nT/m$\sqrt{\text{Hz}}$ at 0.1, 1, 10, and 50 Hz. We also demonstrate the gradiometer performance by measuring the field gradient induced from a current-carrying long straight wire in ambient (outside the magnetic shield) conditions.

2. Experimental Techniques

Al$_2$O$_3$(60 nm)/Ta(5 nm)/Permalloy (Ni$_{80}$Fe$_{20}$, Py)(50 nm)/Ta(5 nm) films are sputter deposited on Si/SiO$_2$(naturally oxidized) wafers by ion beam sputtering (Intelvac Nanoquest I, Ontario, Canada). Elliptical shapes with a major axis (*a*) length of 5 mm and minor axis (*b*) length of 0.833 mm are patterned via photo-lithography, ion milling, and wet etch processes. Gold electrical contact pads of ~1.5 times the thickness of Py are deposited and patterned via photo-lithography and lift-off processes in a second stage. Figure 1 shows a schematic diagram of an EPHEG including the configuration and dimensions of its electrical contacts. Sensitivity is measured in zero dc field by measuring the PHE signal with an ac magnetic field (100–200 nT) generated by a home-built, calibrated solenoid kept inside a magnetic shield (AMUNEAL MFG CORP, Philadelphia, PA, USA). For noise characterization and sensitivity measurements, the sensor is excited along the magnetic easy axis (long axis of the ellipse) with an ac current (1210 Hz) of different amplitudes employing a PXI-5421 function generator. Using an ultra-low noise transformer-matched amplifier (TMA, home built) [21], the transverse PHE voltage is amplified and digitized using a 24-bit sigma-delta analog to digital converter model PXIe 4464, from National Instruments. Noise measurements are performed inside a 3-layer Mu-metal magnetic shield to mitigate the effect of the ambient field and electromagnetic interferences. Gradient sensitivity and equivalent gradient magnetic noise are calculated from the measured sensitivity and voltage noise spectral densities of different voltage pairs, respectively. For testing and demonstration, the magnetic field from a long thin straight wire (length ~1.5 m, radius ~0.1 mm) carrying an ac current (5 Hz) is measured using the same instruments and electronics used for noise measurements in an open environment (outside the magnetic shield) and compared to the theoretical values calculated by Ampere's law. All measurements are performed at room temperature.
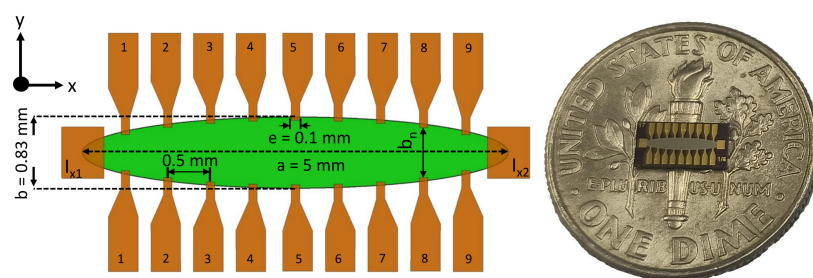

Figure 1. (**left**) Schematics of EPHEG geometry (not to scale). The orange regions are gold electrical contact pads. The long and short axes of the ellipse are labeled as *a* and *b*, respectively. The sensor is excited between I$_{x1}$ and I$_{x2}$, and the transverse signal is measured across any of the parallel 9 voltage pairs (marked from 1 to 9). b_n is the distance between voltage pairs *n*. (**right**) Photograph of a sensor on a dime as a size reference.

3. Equivalent Magnetic Noise Characterizations

Our EPHEG consists of nine parallel voltage pairs that are equally spaced along the x-axis with a separation of 0.5 mm between each pair (Figure 1). To explore the position dependence of EMN, we measured the sensitivity (S_y) and noise at all voltage pairs.

The S_y of the EPHEG is defined as the ratio between the transverse voltage V_y (voltage across the parallel voltage pairs 1 to 9 in Figure 1) and the in-plane magnetic field B applied along the short axis of the ellipse given a current I_x flowing between I_{x1} and I_{x2} (Figure 1). For magnetic fields much smaller than the magnetic anisotropy field, S_y in V/T is given by [22]:

$$S_y = \frac{V_y}{B} = I_x \cdot \frac{\Delta\rho}{t} \cdot \frac{1}{H_{eff}} = I_x \cdot \Delta R \cdot \frac{1}{H_{eff}} \tag{1}$$

where $\Delta\rho$ is $(\rho_\parallel - \rho_\perp)$, $\rho_\parallel$ and $\rho_\perp$ are the resistivities when the magnetization is parallel and perpendicular to the current, t is the film thickness, ΔR is $\frac{\Delta\rho}{t}$, and H_{eff} is the effective anisotropy field, which is the sum of the shape-induced anisotropy and growth-induced anisotropy [23].

S_y for all the nine parallel voltage pairs is measured for several excitation currents and is found to be linear with the excitation (FIG. S1 in the supporting information (SI)). S_y for $I_x \sim 130$ mA (peak) and different voltage pairs is listed in Table 1. We note a systematic change in S_y; S_y is maximum for the middle voltage pairs, and it decreases towards edge pairs. Based on Equation (1), S_y depends inversely on H_{eff}. H_{eff} is lowest at the middle voltage pair (pair 5) and increases gradually towards the edge pairs. The reduction in S_y ($\sim$21% reduction from the middle to edge pair), however, is mostly due to the reduction in ΔR rather than the nominal increase in H_{eff} (only $\sim$ 6%).

R_y (transverse resistance) is at a maximal value at the middle voltage pair and decreases towards the edges due to the increase in the transverse distance (b_n) between the parallel voltage pairs (see the schematic in Figure 1). R_y, H_{eff}, ΔR, and b_n for different voltage pairs are also tabulated in Table 1. The two-probe longitudinal resistance (R_x) and AMR ratio of the film are $\sim$38 Ω and $\sim$1.9 %, respectively.

Equivalent magnetic noise (EMN or B_{eq}) is defined as follows [21,22]:

$$B_{eq}(f) = \frac{e_\Sigma(f)}{S_y} \tag{2}$$

where S_y and e_Σ are the sensitivity (given by Equation (1)) and total noise spectral density, respectively. e_Σ has different contributions from $1/f$, Johnson (thermal), and preamplifier noises and can be expressed as follows [21]:

$$e_\Sigma(f) = \sqrt{I_x^2 R_x^2 \frac{\delta_H}{N_c \cdot Vol \cdot f^\alpha} + 4k_B T R_y + e_{amp}^2} \tag{3}$$

where δ_H is the Hooge parameter [24]. N_C is Permalloy's free electron density of (1.7×10^{29}/m^3). Vol is the sensor's effective volume, where the electrons contribute to the conduction process in a homogeneous sample. f is the frequency. α is a constant. k_B is the Boltzmann constant. T is the temperature of the sensor. R_y is the resistance across the voltage terminals, and e_{amp} is the total noise of the TMA [21]. B_{eq} is obtained by measuring S_y and e_Σ separately [22].

Each EMN vs. frequency data between 0.1 and 100 Hz is fitted with $B_{eq}(f) = \sqrt{c_0^2 + \left(\frac{c_1}{f^\beta}\right)^2}$ (where c_0, c_1, and β are fit parameters [17]). From the fit, EMN at a specific frequency is extracted. EMN for different voltage pairs with an excitation current of $\sim$ 130 mA is shown in Figure 2 for four different frequencies. It can be seen that the best EMNs are in the middle voltage pairs and can be attributed to the observed high sensitivities and comparatively larger effective volumes (due to larger b_n). Similar changes in EMN with voltage-pair positions are also seen for lower excitation (Table S1 in the SI). The best EMNs measured are $\sim$29 pT/$\sqrt{\text{Hz}}$, $\sim$62 pT/$\sqrt{\text{Hz}}$, $\sim$279 pT/$\sqrt{\text{Hz}}$, and $\sim$1322 pT/$\sqrt{\text{Hz}}$ at 50, 10,

1, and 0.1 Hz, respectively, for voltage pair number 5. The obtained EMNs closely resemble those in our previous study with respect to similar thickness (50 nm) elliptical PHE sensors where we explored the thickness dependence of EMNs [17].

Table 1. Typical values of R_y, H_{eff}, S_y (for I_x = ~130 mA (peak)), ΔR, and b_n for different parallel voltage-pairs of EPHEG.

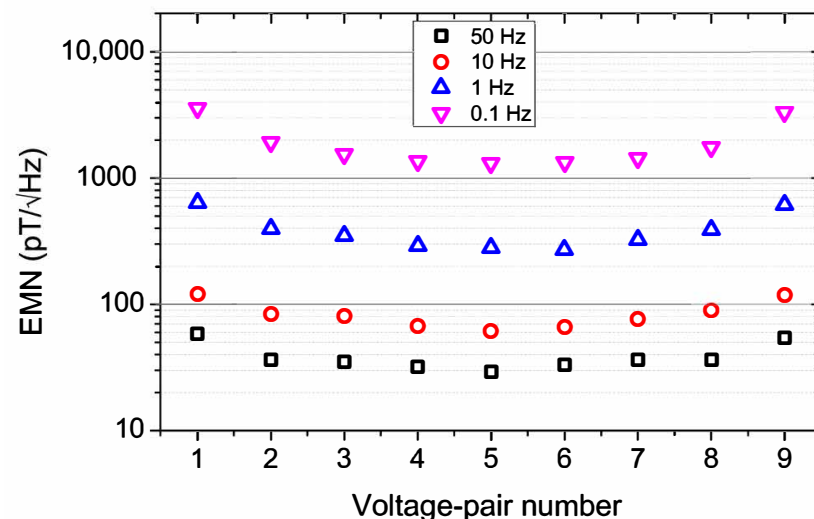| V-Pair No:	R_y (Ω)	H_{eff} (Oe)	S_y (V/T)	ΔR (Ω)	b_n (m)
1	10.05	5.68	17.83	0.0778	4.200×10^{-4}
2	11.14	5.44	22.43	0.0938	5.866×10^{-4}
3	11.53	5.43	23.06	0.0964	6.837×10^{-4}
4	11.57	5.35	23.62	0.0973	7.365×10^{-4}
5	11.79	5.35	23.68	0.0975	7.533×10^{-4}
6	11.61	5.43	23.39	0.0974	7.365×10^{-4}
7	11.49	5.46	23.02	0.0966	6.837×10^{-4}
8	11.07	5.52	22.70	0.0966	5.866×10^{-4}
9	10.12	5.66	18.01	0.0781	4.200×10^{-4}

Figure 2. Plot showing the variation of EMN with the position of the voltage pairs for 50, 10, 1, and 0.1 Hz frequencies and for the highest excitation current of ~130 mA.

4. Equivalent Gradient Magnetic Noise

Our EPHEG with nine voltage pairs can be treated as an array of nine sensors that are placed linearly at 0.5 mm separation between each pair. Considering that the noise measurements are performed in a three-layer magnetically shielded environment, and by employing extremely low noise TMA, the noise sources of any two voltage pairs can be approximated to be completely uncorrelated. The equivalent gradient magnetic noise (gradient resolution, EGMN, or $grad\_B_{eq}$) of two sensors with noise sources that are uncorrelated can be defined as follows.

$$grad\_B_{eq} = \frac{Total\ voltage\ spectral\ noise\ density(f)}{Gradient\ sensitivity} \tag{4}$$

Here, the total voltage spectral noise density (TVSND) can be calculated from individual voltage spectral noise densities (VSNDs) of the two separate sensors as follows:

$$TVSND(f) = \sqrt{VSND_1{}^2(f) + VSND_2{}^2(f)} \tag{5}$$

where $VSND_1$ and $VSND_2$ are the voltage spectral noise densities of sensors 1 and 2, respectively, in $V/\sqrt{Hz}$. The denominator gradient sensitivity (GS) in Equation (4) is the sensitivity towards the gradient field and is defined as follows:

$$GS = \left| \frac{B_1 \cdot S_{y1} - B_2 \cdot S_{y2}}{gradB} \right| \tag{6}$$

where B_1 and B_2 are the magnetic field acting on sensors 1 and 2, and S_{y1} and S_{y2} are their respective sensitivities in V/T. $gradB$ is the magnetic field gradient in T/m.

Equation (6) can be rewritten as follows:

$$GS = \left| \Delta d \cdot S_{y1} + \frac{B_2(S_{y1} - S_{y2})}{gradB} \right| \tag{7}$$

where Δd is the distance between the sensors. Equation (7) shows that GS depends both on the strength of the magnetic field and the gradient field. GS does not depends on the field strength only when both sensors have the same sensitivity: $S_{y1} = S_{y2}$. Selecting a pair of leads with a larger distance will result in higher gradiometer sensitivity. On the contrary, as this distance increases, the capability of the gradiometer to reject interferences generated by other sources of field decreases. This is an important parameter, for example, in real-world scenarios where many sources of interference are present [25]. The multi-lead approach applied with this sensor allows the user to select an optimal sensitivity/rejection configuration that is most applicable to his specific use case. In the case of EPHEG, for obtaining a better GS, we choose two voltage pairs that are farther apart as possible and have the same or very similar S_y. From Table 1, it is clear that S_y of voltage pairs that are relatively at the same positions from the middle of the sensor have similar sensitivities; i.e., voltage pairs 1–9, 2–8, 3–7, and 4–6 have similar sensitivities. Out of these 4 voltage pairs, 1–9 are the farthest pairs and are expected to provide the highest GS and subsequently the best EGMN.

From the S_y of each voltage pair measured for the same excitation, GS is calculated for two voltage pairs having similar sensitivities for an arbitrary constant ΔB of 1 nT ($\Delta B = B_1 - B_2$, B_1 and B_2 are the magnetic field at positions 1 and 2, respectively). TVSND is calculated from the respective VSNDs according to Equation (5) and EGMN is calculated. The calculated frequency dependence of EGMN is fitted with the following:

$$grad\_B_{eq}(f) = \sqrt{a_0^2 + \left(\frac{a_1}{f^\gamma}\right)^2} \tag{8}$$

where a_0, a_1, and γ are fit parameters. Figure 3 shows the EGMN vs. frequency for four different dual voltage pairs. For clarity, data and fit together are shown only for the 1–9 dual voltage pairs, and for all others, only the fit according to Equation (8) is shown. As expected, the best EGMN is obtained when measurement voltage pairs are the farthest apart. The EGMN obtained are ~958, ~192, ~51, ~26, and ~25 nT/m$\sqrt{Hz}$ (pT/mm $\sqrt{Hz}$) at 0.1, 1, 10, 50, and 100 Hz, respectively, with fit parameters a_0, a_1, and γ as 3.76×10^{-9}, 4.43×10^{-8}, and 0.69, respectively.

In comparison with other gradiometers, SQUID-based gradiometers have the best reported gradient field resolution <100 fT/m$\sqrt{Hz}$ followed by atomic magnetometers with <10 pT/m$\sqrt{Hz}$ [26–28]. Fluxgate and magnetoelectric gradiometers reported gradient resolutions <1 nT/m$\sqrt{Hz}$ [29–31]. If we compare the EGMN of a fluxgate gradiometer with baselines of 100 mm [29] and 600 mm [30], they have 0.52 nT/m/$\sqrt{Hz}$ and 0.03 nT/m/$\sqrt{Hz}$ gradient resolutions, respectively, and they are at least two orders higher than our EPHEG's EGMN. However, the reported baselines of these sensors are several times higher than that of our EPHEG sensor, which has a maximum baseline of 4 mm and a minimum baseline of 0.5 mm. The EMN of our EPHEG 's middle pair is 29 pT/$\sqrt{Hz}$, which is better than or within the range of many high-end MEMS fluxgate sensors of smaller size [32,33]. However, the very small baseline of EPHEG has a negative impact on the overall EGMN.

To demonstrate the performance of the EPHEG, the field gradient from an ac current (1 mA, 5 Hz) carrying a long thin straight wire (length ∼1.5 m) is measured in the ambient conditions (outside the magnetic shield) and compared with the theoretical values. For measurements, a calibrated EPHEG is placed near the wire such that the field lines from the wire are in-plane and perpendicular to the long axis of the sensor, as shown schematically in the inset of Figure 4. Starting from a position very close to the wire, the EPHEG is moved (in 4 mm steps) radially outwards on a rail that has precision control on the lateral movements. At each position, the magnetic field is measured by the five different voltage pairs (five alternate pairs covering a total distance of 4 mm) separately with a bandwidth of 0.1 Hz. After measuring all five pairs at a position, the sensor is moved radially outwards 4 mm to a new position and all five pairs are measured again. This procedure is repeated to obtain the field vs. distance plot shown in Figure 4. The error bar on each measurement point represents the standard deviation of ten measurements, and the experimentally measured magnetic fields agree well with the theoretical field values. The lowest gradient field calculated from this measurement is ∼100 nT/m at ∼40 mm.
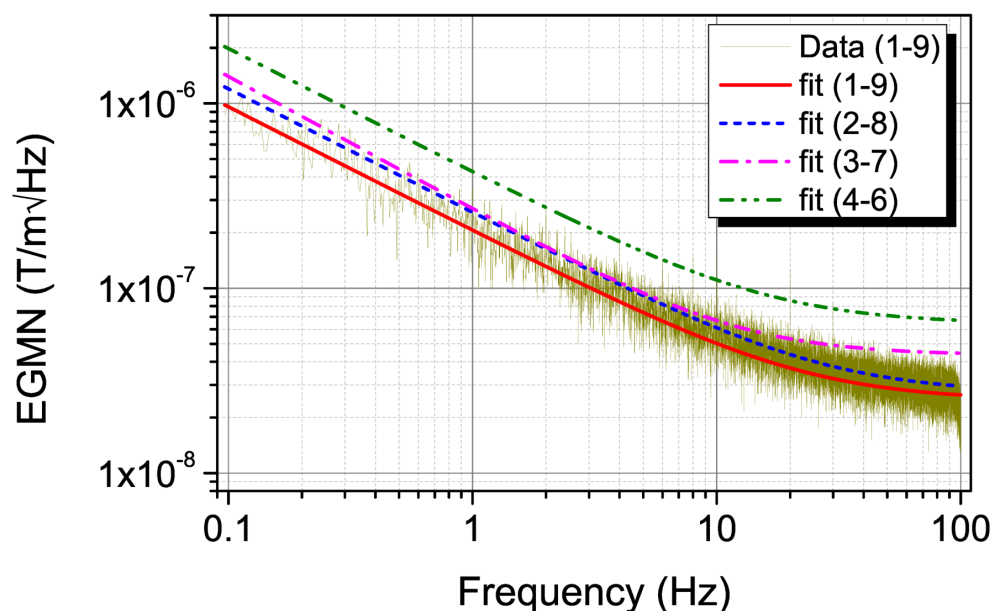

Figure 3. Frequency– dependence of EGMN of 4 voltage pairs 1–9, 2–8, 3–7 and 4–6. Data and fit according to Equation (8) are shown only for the 1-9 voltage pairs. For clarity, only the fit is shown for remaining pairs.

The gradient field resolution improves with the increase in the baseline, and in applications where the gradient field is relatively homogeneous in the sensor's volume, measurement errors can be reduced by averaging the output of several sensor pairs [34,35]. To find out the performance limit of EPHEG, the magnetic field is measured by five different voltage pairs (averaging 20 measurements at each voltage pair) that are separated 1 mm apart (i.e., alternate voltage pairs) covering a total length of 4 mm at a distance of ∼ 40 mm from the wire. At this distance, the magnetic field variation with radial distance from the wire can be approximated to be linear and the slope will give the field gradient. Figure 5 shows the magnetic field from a wire carrying 0.2 mA and 0.4 mA measured along with linear fits. We define the limit of the measurement when the slope of the experimental curve deviates ±10% from the slope of the theoretical one. Accordingly, the lowest magnetic field gradient measured is ∼20 nT/m (slope = −0.0254 nT/mm) for 0.2 mA and ∼40 nT/m (slope = −0.045 nT/mm) for 0.4 mA. In terms of linear fit errors, measuring five pairs has a nominal advantage over measuring two pairs. These values are higher than the EGMN determined for two voltage pairs inside the magnetic shield and the difference could be attributed to the harsh measurement environment. Below 0.2 mA, even though the sensor was able to sense the magnetic field, the gradient field

calculation is erroneous, and for excitations below 0.1 mA, the signal was below the noise floor. Lower bandwidth measurements utilizing all nine voltage pairs are expected to improve these results.

A comparison of gradient field detectivity of several different types of gradiometers by converting a uniform field sensor to a gradiometer of baseline of l cm is reported by J. Javor et al. [14]. Notably, the detectivity of the EPHEG is within the range of the microelectromechanical system (MEMS)[14], Hall effect [36], Fluxgate [19,37], and the majority of magnetoresistive gradiometers [14]. Since our EPHEG can sense the magnetic field at different positions simultaneously, it can find applications in bio-magnetic sensing [38,39], drug delivery [40,41], and other fields where the speed and flow rate of the bio-magnetic particles need to be determined.
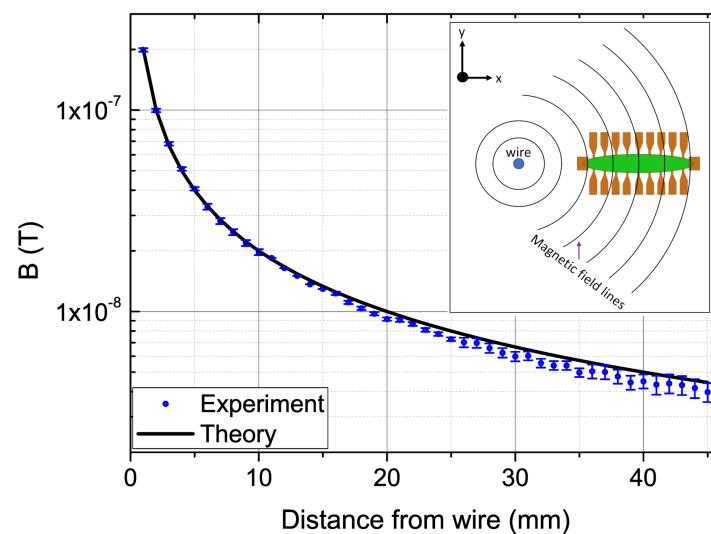

Figure 4. The variation of the magnetic field from a current-carrying wire with a distance from the wire (measured outside the magnetic shield) with an EPHEG along with the calculated magnetic field. The standard deviation of 10 measurements is presented as the error at each point. The inset depicts the schematics of the measurement setup. The current-carrying wire is in the z-direction perpendicular to the plane of the figure.
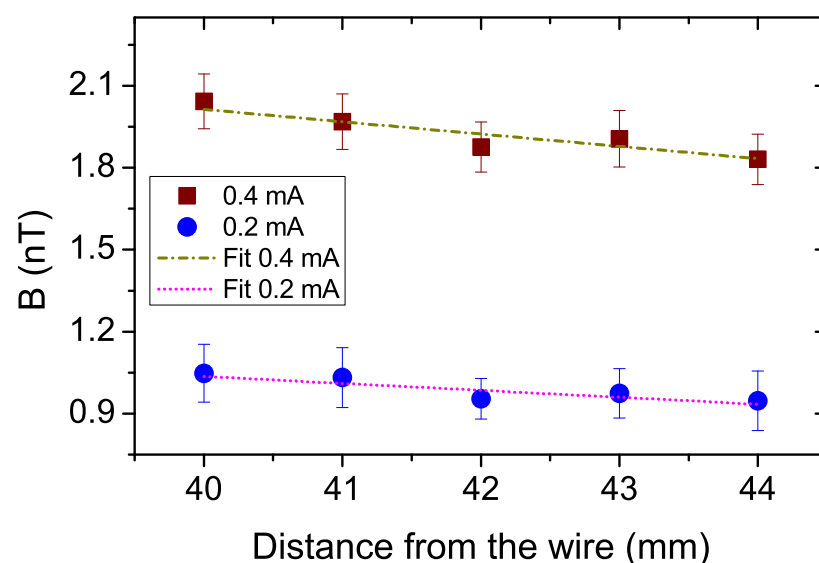

Figure 5. The magnetic field from a wire carrying 0.2 mA and 0.4 mA measured at a distance of ~40 mm using five voltage pairs. The error bar shown for each data point represents the standard deviation of 20 measurements.

5. Summary

In summary, we report the fabrication and performance of a permalloy-based elliptical planar Hall effect magnetic field gradiometer with nine field-sensing positions. Using two field sensing positions with a baseline of 4 mm, it can measure the magnetic field gradients with equivalent gradient magnetic noises of $\sim$958, $\sim$192, $\sim$51, and $\sim$26 nT/m$\sqrt{\text{Hz}}$ (pT/mm$\sqrt{\text{Hz}}$) at 0.1, 1, 10, and 50 Hz, respectively. We demonstrate the performance of the EPHEG by measuring the field gradient from a current-carrying wire using five voltage pairs with a minimum detectivity of $\sim$20 nT/m in ambient conditions outside the magnetic shield. Our simple, low-cost, high-resolution, and small-footprint gradiometer is expected to be highly useful in measuring gradient fields in confined spaces.

Supplementary Materials: The following supporting information can be downloaded at: https://www.mdpi.com/article/10.3390/mi13111898/s1. Figure S1: Excitation current vs Sensitivity (S_y) plot for different excitation currents for all the 9-voltage pairs showing linear dependency. For clarity, only one linear fit is shown (for pair number 9). Table S1: EMNs for 2 different excitation currents for the 9-voltage pairs for 50, 10, 1 and 0.1 Hz frequencies.

Author Contributions: Conceptualization, H.N., L.K., A.G. and M.S.; methodology, H.N. and M.S.; software, H.N., S.A. and M.S.; validation, H.N. and M.S.; investigation, H.N. and M.S.; data curation, H.N.; writing—original draft preparation, H.N.; writing—review and editing, H.N., L.K., A.G., S.A. and M.S.; visualization, H.N.; supervision, L.K.; project administration, L.K. All authors have read and agreed to the published version of the manuscript.

Data Availability Statement: Not applicable.

Conflicts of Interest: The authors declare no conflict of interest.

References

1. Kim, H.; Golynsky, A.; Golynsky, D.; Yu, H.; von Frese, R.; Hong, J. New Magnetic Anomaly Constraints on the Antarctic Crust. *J. Geophys. Res. Solid Earth* **2022**, *127*, e2021JB023329. [CrossRef]
2. Chen, C.H.; Chen, P.W.; Chen, P.J.; Liu, T.H. Indoor Positioning Using Magnetic Fingerprint Map Captured by Magnetic Sensor Array. *Sensors* **2021**, *21*, 5707. [CrossRef]
3. Včelák, J.; Ripka, P.; Kubik, J.; Platil, A.; Kašpar, P. AMR navigation systems and methods of their calibration. *Sens. Actuator A* **2005**, *123*, 122–128. [CrossRef]
4. Ausserlechner, U. The optimum layout for giant magneto-resistive angle sensors. *IEEE Sens. J.* **2010**, *10*, 1571–1582. [CrossRef]
5. Musuroi, C.; Oproiu, M.; Volmer, M.; Neamtu, J.; Avram, M.; Helerea, E. Low field optimization of a non-contacting high-sensitivity GMR-based DC/AC current sensor. *Sensors* **2021**, *21*, 2564. [CrossRef]
6. Ripka, P.; Mlejnek, P.; Hejda, P.; Chirtsov, A.; Vyhnánek, J. Rectangular array electric current transducer with integrated fluxgate sensors. *Sensors* **2019**, *19*, 4964. [CrossRef]
7. Barroso, T.G.; Martins, R.C.; Fernandes, E.; Cardoso, S.; Rivas, J.; Freitas, P.P. Detection of BCG bacteria using a magnetoresistive biosensor: A step towards a fully electronic platform for tuberculosis point-of-care detection. *Biosens. Bioelectron.* **2018**, *100*, 259–265. [CrossRef]
8. Li, Y.; Cheng, H.; Alhalili, Z.; Xu, G.; Gao, G. The progress of magnetic sensor applied in biomedicine: A review of non-invasive techniques and sensors. *J. Chin. Chem. Soc.* **2021**, *68*, 216–227. [CrossRef]
9. Mooney, J.W.; Ghasemi-Roudsari, S.; Banham, E.R.; Symonds, C.; Pawlowski, N.; Varcoe, B.T. A portable diagnostic device for cardiac magnetic field mapping. *Biomed. Phys. Eng. Express* **2017**, *3*, 015008. [CrossRef]
10. Kim, J.; Kumar, R.; Bandodkar, A.J.; Wang, J. Advanced materials for printed wearable electrochemical devices: A review. *Adv. Elect. Mater.* **2017**, *3*, 1600260. [CrossRef]
11. Melzer, M.; Mönch, J.I.; Makarov, D.; Zabila, Y.; Cañón Bermúdez, G.S.; Karnaushenko, D.; Baunack, S.; Bahr, F.; Yan, C.; Kaltenbrunner, M.; et al. Wearable magnetic field sensors for flexible electronics. *Adv. Mater.* **2015**, *27*, 1274–1280. [CrossRef]
12. Jucevičius, M.; Ožiūnas, R.; Narvydas, G.; Jegelevičius, D. Permanent magnet tracking method resistant to background magnetic field for assessing jaw movement in wearable devices. *Sensors* **2022**, *22*, 971. [CrossRef]
13. Feiner, R.; Dvir, T. Tissue–electronics interfaces: from implantable devices to engineered tissues. *Nat. Rev. Mater.* **2017**, *3*, 17076. [CrossRef]
14. Javor, J.; Stange, A.; Pollock, C.; Fuhr, N.; Bishop, D.J. 100 pT/cm single-point MEMS magnetic gradiometer from a commercial accelerometer. *Microsyst. Nanoeng.* **2020**, *6*, 71. [CrossRef]

15. Lim, B.; Mahfoud, M.; Das, P.T.; Jeon, T.; Jeon, C.; Kim, M.; Nguyen, T.K.; Tran, Q.H.; Terki, F.; Kim, C. Advances and key technologies in magnetoresistive sensors with high thermal stabilities and low field detectivities. *APL Mater.* **2022**, *10*, 051108. [CrossRef]

16. Nhalil, H.; Givon, T.; Das, P.T.; Hasidim, N.; Mor, V.; Schultz, M.; Amrusi, S.; Klein, L.; Grosz, A. Planar Hall Effect Magnetometer With 5 pT Resolution. *IEEE Sens. Lett.* **2019**, *3*, 2501904. [CrossRef]

17. Nhalil, H.; Das, P.T.; Schultz, M.; Amrusi, S.; Grosz, A.; Klein, L. Thickness dependence of elliptical planar Hall effect magnetometers. *Appl. Phys. Lett.* **2020**, *117*, 262403. [CrossRef]

18. Tsukamoto, A.; Adachi, S.; Hato, T.; Oshikubo, Y.; Tanabe, K. Design and Fabrication of HTS-SQUID Gradiometer With Imbalance of 10–4 Using a Gradiometric SQUID Structure. *IEEE Trans. Appl. Supercond.* **2022**, *32*, 1600309. [CrossRef]

19. Sui, Y.; Miao, H.; Zhou, Z.; Luan, H.; Wang, Y. Correction and compensation of an airborne fluxgate magnetic tensor gradiometer. *Explor. Geophys.* **2018**, *49*, 726–734. [CrossRef]

20. Mahfoud, M.; Tran, Q.H.; Wane, S.; Ngo, D.T.; Belarbi, E.H.; Boukra, A.; Kim, M.; Elzwawy, A.; Kim, C.; Reiss, G.; et al. Reduced thermal dependence of the sensitivity of a planar Hall sensor. *Appl. Phys. Lett.* **2019**, *115*, 072402. [CrossRef]

21. Grosz, A.; Mor, V.; Amrusi, S.; Faivinov, I.; Paperno, E.; Klein, L. A high-resolution planar Hall effect magnetometer for ultra-low frequencies. *IEEE Sens. J.* **2016**, *16*, 3224–3230. [CrossRef]

22. Grosz, A.; Mor, V.; Paperno, E.; Amrusi, S.; Faivinov, I.; Schultz, M.; Klein, L. Planar hall effect sensors with subnanotesla resolution. *IEEE Mag. Lett.* **2013**, *4*, 6500104. [CrossRef]

23. Mor, V.; Schultz, M.; Sinwani, O.; Grosz, A.; Paperno, E.; Klein, L. Planar Hall effect sensors with shape-induced effective single domain behavior. *J. Appl. Phys.* **2012**, *111*, 07E519. [CrossRef]

24. Gijs, M.; Giesbers, J.; Beliën, P.; Van Est, J.; Briaire, J.; Vandamme, L. 1/f noise in magnetic Ni80Fe20 single layers and Ni80Fe20/Cu multilayers. *J. Magn. Magn. Mater.* **1997**, *165*, 360–362. [CrossRef]

25. McKenna, S.P.; Parkman, K.B.; Perren, L.J.; McKenna, J.R. Response of an electromagnetic gradiometer to a subsurface wire. *IEEE Trans. Geosci. Remote Sens.* **2011**, *49*, 4944–4953. [CrossRef]

26. Song, Z.; Dai, H.; Rong, L.; Dong, H.; Wu, J.; Qiu, L.; Zhang, G.; Wang, Y.; Tao, Q.; Pei, Y.; et al. Noise compensation of a mobile LTS SQUID planar gradiometer for aeromagnetic detection. *IEEE Trans. Appl. Supercond.* **2019**, *29*, 1600205. [CrossRef]

27. Perry, A.; Bulatowicz, M.; Larsen, M.; Walker, T.; Wyllie, R. All-optical intrinsic atomic gradiometer with sub-20 fT/cm/sqrt Hz sensitivity in a 22 μT earth-scale magnetic field. *Opt. Express* **2020**, *28*, 36696–36705. [CrossRef]

28. Limes, M.; Foley, E.; Kornack, T.; Caliga, S.; McBride, S.; Braun, A.; Lee, W.; Lucivero, V.; Romalis, M. Total-field atomic gradiometer for unshielded portable magnetoencephalography. *arXiv* **2020**, arXiv:2001.03534. [CrossRef]

29. Sui, Y.; Li, G.; Wang, S.; Lin, J. Compact fluxgate magnetic full-tensor gradiometer with spherical feedback coil. *Rev. Sci. Instr.* **2014**, *85*, 014701. [CrossRef]

30. Merayo, J.M.; Brauer, P.; Primdahl, F. Triaxial fluxgate gradiometer of high stability and linearity. *Sens. Actuators A* **2005**, *120*, 71–77. [CrossRef]

31. Zhang, M.; Or, S.W. Magnetoelectric transverse gradient sensor with high detection sensitivity and low gradient noise. *Sensors* **2017**, *17*, 2446. [CrossRef]

32. Shen, X.; Teng, Y.; Hu, X. Design of a low-cost small-size fluxgate sensor. *Sensors* **2021**, *21*, 6598. [CrossRef]

33. Wang, Z.; Shen, Y.; Lei, C.; Wang, J.; Zhao, S.; Chen, J.; Chu, Z.; Gao, J. Highly-Sensitive MEMS Micro-Fluxgate Magnetometer. *IEEE Elec. Dev. Lett.* **2022**, *43*, 1327–1330. [CrossRef]

34. Shen, Y.; McLaughlin, K.L.; Gao, J.; Li, M.; Li, J.; Viehland, D. Effective optimization of magnetic noise for a Metglas/Pb (Zr, Ti) O3 magnetoelectric sensor array in an open environment. *Mater. Lett.* **2013**, *91*, 307–310. [CrossRef]

35. Leach, W.M. Fundamentals of low-noise analog circuit design. *Proc. IEEE* **1994**, *82*, 1515–1538. [CrossRef]

36. Jung, G.; Ocio, M.; Paltiel, Y.; Shtrikman, H.; Zeldov, E. Magnetic noise measurements using cross-correlated Hall sensor arrays. *Appl. Phys. Lett.* **2001**, *78*, 359–361.

37. Sui, Y.; Miao, H.; Wang, Y.; Luan, H.; Lin, J. Correction of a towed airborne fluxgate magnetic tensor gradiometer. *IEEE Geosci. Remote. Sens. Lett.* **2016**, *13*, 1837–1841. [CrossRef]

38. Klein, T.; Wang, W.; Yu, L.; Wu, K.; Boylan, K.L.; Vogel, R.I.; Skubitz, A.P.; Wang, J.P. Development of a multiplexed giant magnetoresistive biosensor array prototype to quantify ovarian cancer biomarkers. *Biosens. Bioelectron.* **2019**, *126*, 301–307. [CrossRef]

39. Schutt, J.; Illing, R.; Volkov, O.; Kosub, T.; Granell, P.N.; Nhalil, H.; Fassbender, J.; Klein, L.; Grosz, A.; Makarov, D. Two Orders of Magnitude Boost in the Detection Limit of Droplet-Based Micro-Magnetofluidics with Planar Hall Effect Sensors. *ACS Omega* **2020**, *5*, 20609–20617. [CrossRef] [PubMed]

40. Gul, A.; Tzirtzilakis, E.E.; Makhanov, S.S. Simulation of targeted magnetic drug delivery: Two-way coupled biomagnetic fluid dynamics approach. *Phys. Fluids* **2022**, *34*, 021911. [CrossRef] [PubMed]

41. Shaw, S.; Shit, G.; Tripathi, D. Impact of drug carrier shape, size, porosity and blood rheology on magnetic nanoparticle-based drug delivery in a microvessel. *Colloids Surf. A* **2022**, *639*, 128370. [CrossRef]